Published in "Nature Geoscience 12(8): 650–656, 2019"
which should be cited to refer to this work.

# Last phase of the Little Ice Age forced by volcanic eruptions

**Stefan Brönnimann[1,2]*, Jörg Franke[1,2], Samuel U. Nussbaumer[3,4], Heinz J. Zumbühl[1,2], Daniel Steiner[5], Mathias Trachsel[1,2,6,9], Gabriele C. Hegerl[7], Andrew Schurer[7], Matthias Worni[1,2], Abdul Malik[1,2,10], Julian Flückiger[1,2] and Christoph C. Raible[1,8]**

**During the first half of the nineteenth century, several large tropical volcanic eruptions occurred within less than three decades. The global climate effects of the 1815 Tambora eruption have been investigated, but those of an eruption in 1808 or 1809 whose source is unknown and the eruptions in the 1820s and 1830s have received less attention. Here we analyse the effect of the sequence of eruptions in observations, global three-dimensional climate field reconstructions and coupled climate model simulations. All the eruptions were followed by substantial drops of summer temperature over the Northern Hemisphere land areas. In addition to the direct radiative effect, which lasts 2–3 years, the simulated ocean–atmosphere heat exchange sustained cooling for several years after these eruptions, which affected the slow components of the climate system. Africa was hit by two decades of drought, global monsoons weakened and the tracks of low-pressure systems over the North Atlantic moved south. The low temperatures and increased precipitation in Europe triggered the last phase of the advance of Alpine glaciers. Only after the 1850s did the transition into the period of anthropogenic warming start. We conclude that the end of the Little Ice Age was marked by the recovery from a sequence of volcanic eruptions, which makes it difficult to define a single pre-industrial baseline.**



The period between around 1350 or 1450 and 1850 is often termed the 'Little Ice Age' (LIA). In several regions the LIA was accompanied by glacier advances[1,2]. It might have been initiated by volcanic eruptions[3], but the relative contributions of solar and volcanic forcing remain unclear. Given the regional differences[4] and uncertainties in the mechanism involved, the onset of the LIA is still highly debated[5].

Importantly, the transition from the LIA into the period of anthropogenic warming is also not well understood. After a rather warm phase around 1800, global climate cooled again in the early nineteenth century[6] for several decades, accompanied by pronounced glacier advances in the Alps. Recent work, therefore, dated the start of anthropogenic warming back to the early nineteenth century[7]. However, that several major tropical volcanoes erupted between 1808 and 1835 (note that there is still large uncertainty over these—the 1808 or 1809 eruption, in this paper attributed to December 1808, remains unknown[8] and the attribution of the 1831 eruption was recently questioned[9]), including the well-studied 1815 Tambora eruption, makes the separation between volcanic and anthropogenic contributions difficult. Based on attribution results, a small drop in greenhouse gas levels during the LIA and the subsequent recovery and beginning of the industrial era affected the Northern Hemisphere temperatures[10,11]. The peak cold conditions in the early nineteenth century were dominated by volcanism[11]. However, except for Tambora[12], these eruptions are not well studied, and their contribution to global early nineteenth century climate is unclear.

Here we used an ensemble of global climate field reconstructions based on data assimilation[13] (termed palaeo-reanalysis here (Methods)) and analysed it together with instrumental data[14], existing reconstructions[6,15,16] and climate simulations (HadCM3 and FUPSOL (Methods))[10,17]. We then studied the effects of the volcanic eruptions on different parts of the climate system, which included precipitation in the monsoon regions[16] and Alpine glaciers (see also refs. [18,19]).

## Cold northern extratropical summers

The coldest ten warm seasons (April–September) over the northern extratropical land areas in the period 1750–1900 in the ensemble mean of the palaeo-reanalysis were exclusively post-eruption seasons (Fig. 1a and Methods). Those that followed the early nineteenth century eruptions were on average 0.5 °C cooler than the 30-year period that preceded the sequence of eruptions (1779–1808). Instrumental series (all but one are from Europe) confirm the post-eruption cooling (Fig. 1a), but their long-term trend might be affected by a warm bias due to measurement practices in the early decades[20]. The Crowley et al. temperature reconstruction[6] also shows a predominance of post-volcanic years among the coldest warm seasons (six among the coldest 12 and 12 among the coldest 30 warm seasons) and tracks the palaeo-reanalysis very well. A recovery only occurred around 1850. This is consistent with a sustained global cooling after eruptions in volcanic-only simulations[11] and with new global temperature reconstructions[21].

Anomaly fields for the temperature in the palaeo-reanalysis (Fig. 2), which is well constrained by instrumental, documentary and tree-ring data (indicated by dashed and solid lines) over northern extratropical land areas but little-constrained elsewhere,

[1]Oeschger Centre for Climate Change Research, University of Bern, Bern, Switzerland. [2]Institute of Geography, University of Bern, Bern, Switzerland. [3]Department of Geography, University of Zurich, Zurich, Switzerland. [4]Department of Geosciences, University of Fribourg, Fribourg, Switzerland. [5]Bern University of Teacher Education, Bern, Switzerland. [6]Department of Geology, University of Maryland, College Park, MD, USA. [7]School of Geosciences, University of Edinburgh, Edinburgh, UK. [8]Climate and Environmental Physics, Physics Institute, University of Bern, Bern, Switzerland. [9]Present address: Department of Geography, University of Wisconsin-Madison, Madison, WI, USA. [10]Present address: Grantham Institute – Climate Change and the Environment, Imperial College London, London, UK. *e-mail: stefan.broennimann@giub.unibe.ch

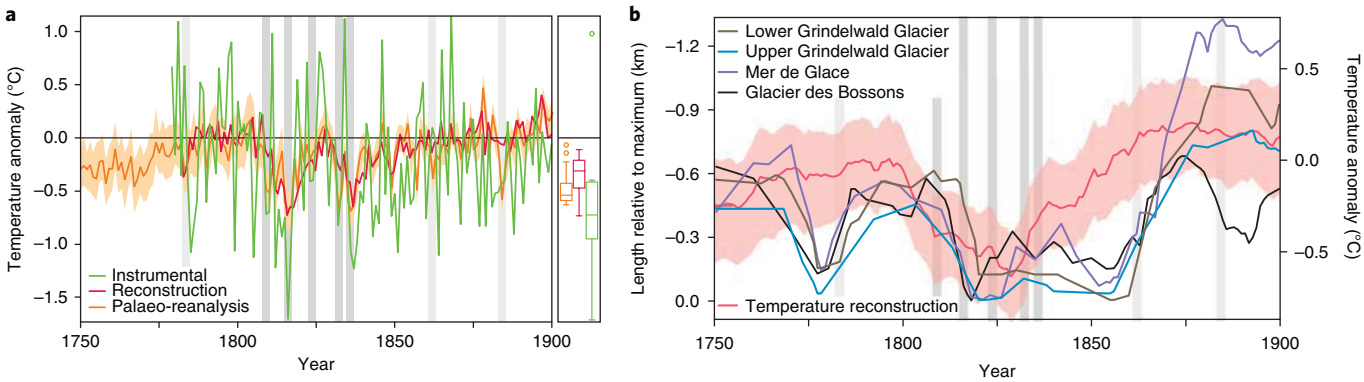


**Fig. 1 | Climate series for the last part of the LIA. a**, Temperature anomalies (with respect to 1779–1808) of northern extratropical land areas (20–90° N) in April–September from the palaeo-reanalysis (the orange line is the ensemble mean and orange shading denotes the 95% ensemble spread) as well as a reconstruction (30–90° N)[6] and the average of 23 early instrumental series (Methods). **b**, Length of four well-documented Alpine glaciers[38–40] relative to the maximum in the displayed period as well as 30 yr running means of Alpine summer temperature from a multiproxy reconstruction[15] (red shading denotes the 95% confidence interval (Methods); the curve is advanced by 5 yr, which approximates the glacier response). The grey bars indicate volcanic eruptions. The box plots with quartiles (whiskers extend to furthest value within 1.5× interquartile range from box) in **a** show the post-volcanic seasons of the five eruptions in the early nineteenth century.

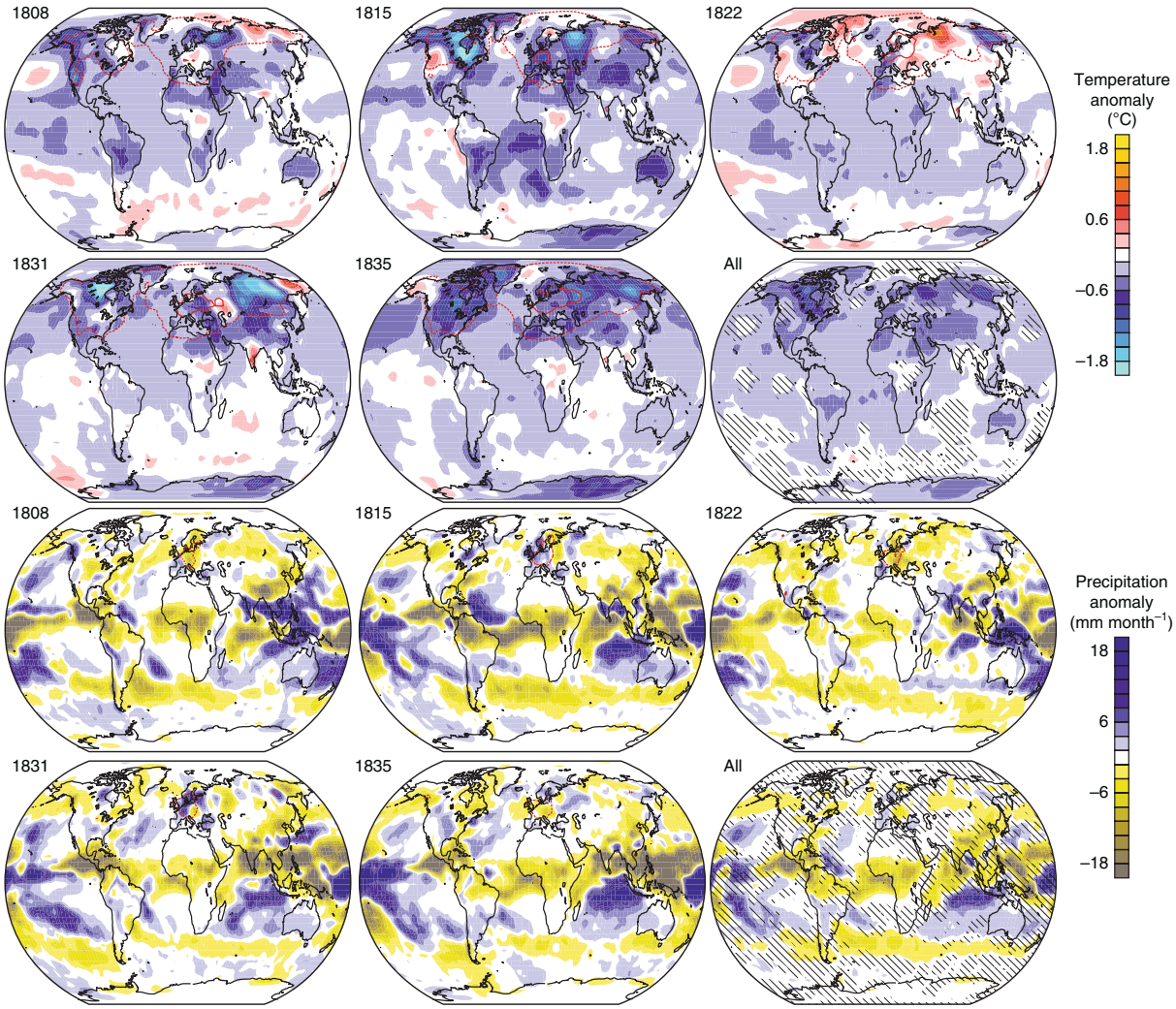


**Fig. 2 | Post-volcanic anomalies in April–September in the palaeo-reanalysis (ensemble mean).** Top two rows, temperature; bottom two rows, precipitation; anomalies are relative to 1779–1808. The solid and dashed red contours indicate areas in which the reduction of the ensemble spread due to the assimilation reaches 75% and 25%, respectively. Eruptions (analysed seasons) are: unknown, December 1808 (1809–1811); Tambora, April 1815 (1815–1817); Galanggung, October 1822 (1823–1824); unknown (Babuyan Claro?), September 1831 (1832–1833); Cosigüina, January 1835 (1835–1837). Panels 'All' show the average over all five eruptions, and hatching indicates where the sign agrees for less than four.

exhibit the expected pattern of radiatively forced change. This includes large-scale cooling over the extratropical land masses in the three years following volcanic eruptions.

Reconstructions of climatic variables also show substantial changes on a decadal scale during these years, as shown in Fig. 1b for a multiproxy reconstruction of summer temperature for the Alps[15]. Even for 30-year averages, a temperature change of 0.65 °C was found between the late eighteenth and early nineteenth centuries, probably related to the coincidence of five strong tropical eruptions (Fig. 1b). This change is highly significant and highlights the difficulty of defining a single preindustrial reference climate[22,23].

## Weak monsoons

With regard to precipitation anomalies after eruptions, the palaeo-reanalysis (Figs. 2 and 3a) shows a decreased rainfall in the African monsoon region immediately following each eruption. This result mainly arises from the model response to the forcing as precipitation is only weakly constrained in the palaeo-reanalysis; it is also found in model studies[24]. Completely independent reconstructions of African dryness back to 1800 based on documentary data (such as lake levels or Nile river flow), although partly infilled, confirm that all post-eruption years (except after the Galanggung eruption 1822) were dry in the African monsoon region[16] (Fig. 3a). According to both data sets the region remained dry during most of the first half of the nineteenth century.

We further analysed other monsoon regions and compared the palaeo-reanalysis with independent observations[25,26]. We found a weakening of all India monsoon rainfall (Fig. 3b) and of the strength of the Australian monsoon that lasted several decades (Fig. 3c; the offset between the curves is due to different standardization periods) in observations. The palaeo-reanalysis, which is largely unconstrained with respect to monsoon precipitation, shows similar multidecadal variability (although no clear post-volcanic signal). Weak monsoons continued through the 1840s and early 1850s. Can such a long-lasting effect be explained climatically?

Ocean memory integrates weather and climate noise[27], and precipitation anomalies in the African monsoon region may trigger decadal dryness by means of land–surface feedback processes[28]. Therefore, a sequence of eruptions that lead to cooling in Europe and land areas globally, as well as drying in Africa and in monsoon regions globally, may lead to persisting effects in the climate system. Thus, we analysed two ensembles of coupled simulations (FUPSOL and HadCM3) to identify persisting climate signals in the oceans. Global annual mean surface air temperatures (Fig. 4c) cool by 0.15–1 °C in the two years following each eruption (note that the 1822 Galanggung eruption was not in the model forcing of either model, and the 1861 Dubbi eruption was only in HadCM3). The differences between the two ensembles reflect different volcanic forcing (as evidenced in the top-of-atmosphere net shortwave radiation (Fig. 4a)) and arguably different sensitivities. In both ensembles, annual mean temperatures of the 1770s to 1800s were only reached again in the 1840s and 1850s.

## Oceanic response

To address the mechanisms for the possible sustained effects of this sequence of eruptions, we analysed surface energy fluxes (Fig. 4b) and upper ocean heat content (Fig. 4d). In response to the decreased short-wave forcing, the upper ocean cools. In a simple mixed-layer deep-ocean model[29], the effect of a volcanic eruption on the mixed layer is expected to decay within about 2–3 years, but mixing into the deep ocean can lead to delayed ('recalcitrant') responses that accumulate between eruptions[29,30]. In our simulations, the global upper ocean (0–700 m) heat content reduced substantially after each eruption, consistent with other simulations[31,32] (the differences between FUPSOL and HadCM3 indicate possible drifts caused by different volcanic histories affecting the centennial time scale[33]).

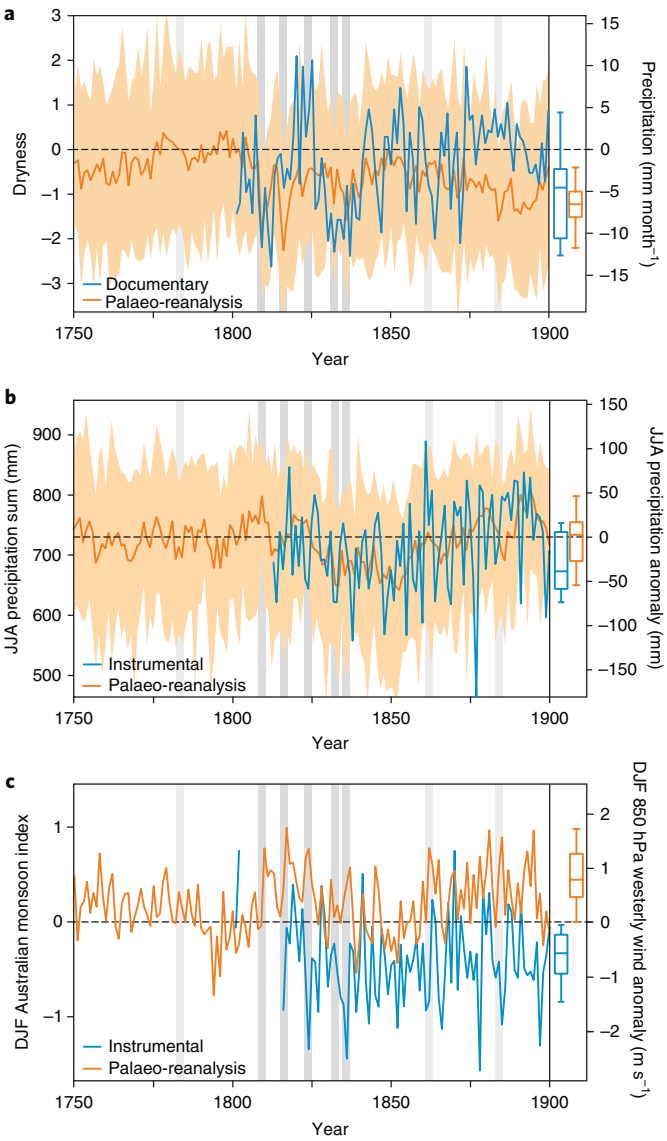


**Fig. 3 | Change in global monsoon systems. a**, Dryness index for the African monsoon region (0–20° N, 20° W to 30° E) from documentary data[16] and precipitation (April–September) in the palaeo-reanalysis in the same area. **b**, All India monsoon rainfall (June–August (JJA)) in instrumental observations[25] and in the palaeo-reanalysis (67–98° E, 5–36° N). **c**, Australian monsoon index (December–February (DJF)) in instrumental observations[26] (number of days with westerly winds at the surface in the region 98–138° E, 5–18° S, standardized relative to 1800–2014) and the 850 hPa westerly wind in the palaeo-reanalysis in the same region. The observations are on the left axes. The palaeo-reanalysis data are on the right axes (orange lines show the ensemble means and orange shading denotes the 95% ensemble spread; not shown in **c** as it fills the panel) and are anomalies from 1779–1808. The bars indicate volcanic eruptions. The box plots (as in Fig. 1) show the post-volcanic seasons of the five early nineteenth century eruptions.

Upper-ocean heat content does not recover to the 1779–1808 value until the 1860s (in FUPSOL) or even the 1930s (in HadCM3). This is consistent with a possible temporary slow-down in sea-level rise in the nineteenth century found in some reconstructions[34].

This is related to changes in oceanic heat uptake. The net surface heat flux (net surface short- and long-wave radiation minus upward sensible and latent heat fluxes (Fig. 4b)) reaches the highest upward

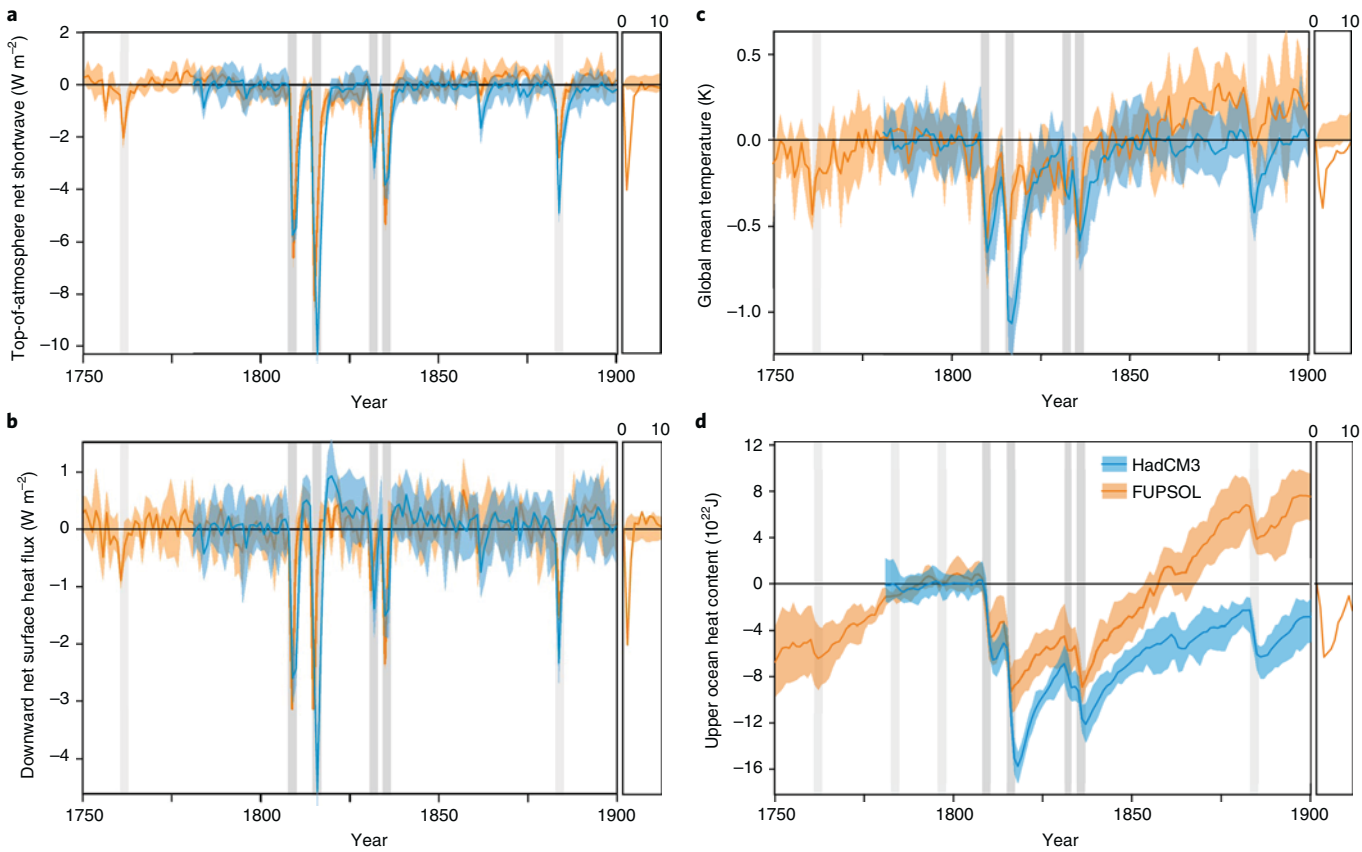


**Fig. 4 | Global annual means of energy fluxes, temperature and ocean heat content in coupled model simulations (ensemble mean and range). a–d**, The top of atmosphere net shortwave flux (**a**), the downward net surface heat flux (**b**), the global mean surface air temperature (**c**) and the global upper ocean heat content (0–700 m) (**d**). Anomalies are relative to 1780–1808. Shading, ensemble range; bars, volcanic eruptions. Insets, composites over all the eruptions in the FUPSOL simulations (1600–2000) for the first ten years, referenced to the year before the eruption (Methods); shading indicates 95% confidence intervals from Monte Carlo simulations.

anomalies (less energy input into the oceans (negative spikes in Fig. 4b)) immediately after the eruptions. The opposite is the case after about three years, when the short-wave forcing ceases. During this recovery phase, oceans take up heat and recharge their heat content, which leads to slight but sustained positive anomalies compared to the years prior to the eruptions. This effect is particularly clear in HadCM3, in which three years after the 1808 and the Tambora eruptions all ten members exhibit an anomalously positive downward heat flux for several years (Fig. 4b). This effect also appears as statistically significant in FUPSOL when composited over all the simulated eruptions (Fig. 4, right insets) and was found in several other models[31,32].

The heat uptake during the recovery phase does not occur in a globally uniform way. Composites for the FUPSOL and HadCM3 simulations for the four modelled early nineteenth century eruptions (Fig. 5) suggest that the equatorial Pacific cooled slightly less than the remaining oceans in the first two years after the eruptions, consistent with other studies[35]. In the subsequent five years, the central equatorial Pacific cooled further as the globe warmed. Although there is a large within-ensemble variability (hatching in Fig. 5) at these locations, the general pattern is consistent with the sea-surface temperature reconstruction that was used to force the palaeoreanalysis[13,36]. Note that this reconstruction was designed to study decadal-to-multidecadal variability, with the shorter-term variability underestimated[37]. This might explain the rather weak signal.

The latter pattern is similar, although not identical, to the Pacific Decadal Oscillation, a dominant climate mode. This suggests that the recovery from volcanic eruptions may resemble internal oceanic variability modes. This makes the separation of forced and unforced climate variability difficult.

## Growing glaciers

Other slow parts of the climate system might also have reacted to the combined effect of five eruptions. Glacier length integrates and delays the primary climatic signal, and thus the volcanic forcing might have contributed to glacier growth. We analysed the length of four well-observed Alpine glaciers (Fig. 1b, note the inverted *y* axis)[38–40]. Concurrent with the drop in warm-season temperature in the early nineteenth century, three of the four glaciers reached their maximum length around 1820. This is consistent with a reduced melting due to volcanic summer cooling. All the glaciers showed a second maximum in the 1850s (which for one glacier was longer than the first). By that time, the Alpine temperature had already increased (Fig. 1b). However, based on bandpass-filtered subdaily pressure measurements along a North–South transect in Europe (Methods) we found an intensification and southward shift of cyclonic activity (predominantly in the summer and autumn), which we interpret as an intensification and a southward shift of the Atlantic–European cyclone track during the late 1830s, 1840s and into the 1850s (Supplementary Fig. 1). This is also mirrored in increased precipitation[41,42] and in multidecadal changes in the daily Alpine weather types derived from observations. Flood-prone, cyclonic types during the warm season were more frequent from the mid-1810s until around 1880 than before or after this period[42]. The second glacier advance is thus consistent with the observed climatic changes, but was arguably not a pure temperature effect.

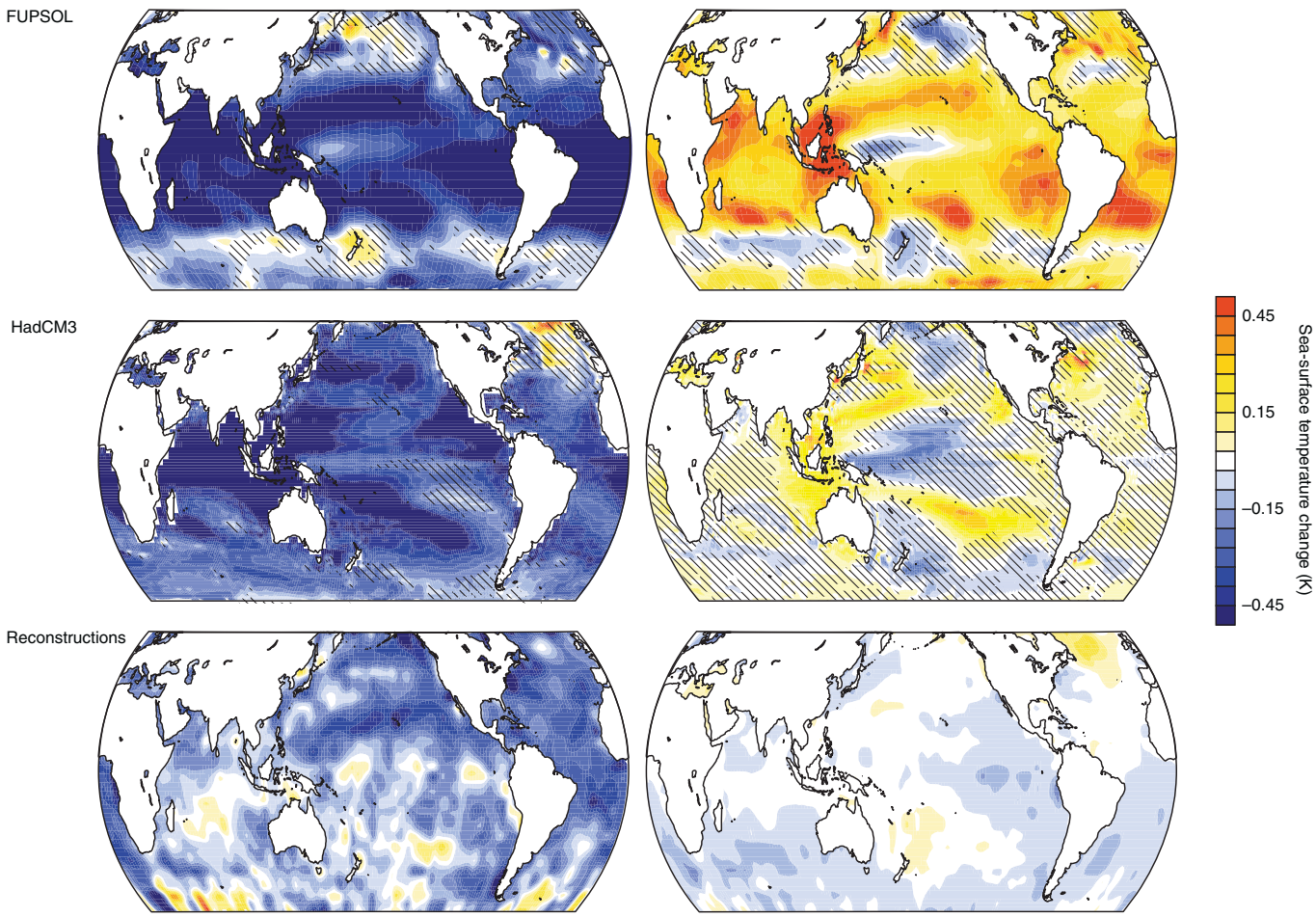


**Fig. 5 | Annual mean sea-surface temperature changes in HadCM3, FUPSOL and reconstructions following the four volcanic eruptions of 1808, 1815, 1831 and 1835.** Left, years 1 and 2 relative to 1780–1808; right, years 3–7 relative to years 1 and 2. Hatching indicates that less than eight out of ten members (less than three out of four for FUPSOL) agree in sign.



## Southward shift of circulation

A southward shift of the Atlantic–European cyclone track after volcanic eruptions was found in a previous study and related to a weak African monsoon and consequent weakening of the Atlantic–European Hadley cell[43]. After the last of the five-early nineteenth century eruptions, the weak monsoons and southward-shifted circulation persisted for ten years (Fig. 3 and Supplementary Fig. 1). A southward shift of the northern subtropical jet and of the downwelling branch of the northern Hadley cell in the 1830s to 1850s was also found in a zonal average in the palaeo-reanalysis during the boreal warm season (Supplementary Fig. 2). Furthermore, a recent reconstruction of the northern tropical belt boundary based on tree-ring width also displayed a southward shift in the first half of the nineteenth century[44]. Hence, daily pressure observations, the palaeo-reanalysis and a tree-ring-based reconstruction agree with each other and suggest a southward shift of circulation.

A possible cause for this is a negative phase of the Atlantic Multidecadal Oscillation in the 1830s to 1850s, according to reconstructions[36,45]. This might have contributed to weak African[46] and Indian monsoons[47] and to the southward shift of the northern tropical belt[48]. To what extent the change in the Atlantic Multidecadal Oscillation itself was related to the atmospheric circulation changes triggered by the eruptions, as was suggested for later eruptions[49], or to the decreased solar activity during the Dalton minimum[50,51], or whether the Atlantic Multidecadal Oscillation change was entirely unrelated to these forcings, remains to be clarified.

Our analysis shows that the last phase of the LIA was characterized by large decadal-to-multidecadal climatic fluctuations[21]. In particular, a sequence of five volcanic eruptions within 28 years caused widespread global cooling, drying in central Africa and a weakening of global monsoons, among other effects. The cooling in Europe favoured the growth of Alpine glaciers. The global temperature increase that started in the late 1830s therefore primarily reflects the recovery of the global climate system from a sequence of eruptions, with possibly a minor contribution from anthropogenic greenhouse gases[7]. From the late nineteenth and early twentieth century onward, the greenhouse gas increase dominated the long-term trend[11,52]. Additional pronounced internal climate variability then catapulted global climate out of the LIA and into a first warm phase, the early twentieth century warming[42,53].

## Online content

Any methods, additional references, Nature Research reporting summaries, source data, statements of code and data availability and associated accession codes are available at https://doi.org/10.1038/s41561-019-0402-y.

Received: 12 March 2019; Accepted: 6 June 2019;
Published online: 24 July 2019

## References


1. Zumbühl, H. J., Steiner, D. & Nussbaumer, S. U. 19th century glacier representations and fluctuations in the central and western European Alps: an interdisciplinary approach. *Glob. Plan. Change* **60**, 42–57 (2008).
2. Leclercq, P. W. et al. A data set of worldwide glacier length fluctuations. *Cryosphere* **8**, 659–672 (2014).
3. Miller, G. H. et al. Abrupt onset of the Little Ice Age triggered by volcanism and sustained by sea-ice/ocean feedbacks. *Geophys. Res. Lett.* **39**, L02708 (2012).
4. PAGES 2k Consortium.Continental-scale temperature variability during the last two millennia. *Nat. Geosci.* **6**, 339–346 (2013).
5. Masson-Delmotte, V. et al. in *Climate Change 2013: The Physical Science Basis* (eds Stocker, T. F. et al.) 383–464 (Cambridge Univ. Press, 2013).
6. Crowley, T. J., Obrochta, S. P. & Liu, J. Recent global temperature 'plateau' in the context of a new proxy reconstruction. *Earth's Future* **2**, 281–294 (2014).
7. Abram, N. J. et al. Early onset of industrial-era warming across the oceans and continents. *Nature* **536**, 411–418 (2016).
8. Guevara-Murua, A., Williams, C. A., Hendy, E. J., Rust, A. C. & Cashman, K. V. Observations of a stratospheric aerosol veil from a tropical volcanic eruption in December 1808: is this the unknown ∼1809 eruption? *Clim. Past* **10**, 1707–1722 (2014).
9. Garrison, C. S., Kilburn, C. R. J. & Edwards, S. J. The 1831 eruption of Babuyan Claro that never happened: has the source of one of the largest volcanic climate forcing events of the nineteenth century been misattributed? *J. Appl. Volcanol.* **7**, 8 (2018).
10. Schurer, A., Tett, S. F. B. & Hegerl, G. C. Small influence of solar variability on climate over the last millennium. *Nat. Geosci.* **7**, 104–108 (2014).
11. Schurer, A., Hegerl, G. C., Mann, M., Tett, S. F. B. & Phipps, S. Separating forced from chaotic variability over the last millennium. *J. Clim.* **26**, 6954–6973 (2013).
12. Raible, C. C. et al. Tambora 1815 as a test case for high impact volcanic eruptions: Earth system effects. *WIREs Clim. Change* **7**, 569–589 (2016).
13. Franke, J., Brönnimann, S., Bhend, J. & Brugnara, Y. A monthly global paleo-reanalysis of the atmosphere from 1600 to 2005 for studying past climatic variations. *Sci. Data* **4**, 170076 (2017).
14. Lawrimore, J. H. et al. An overview of the global historical climatology network monthly mean temperature data set, version 3. *J. Geophys. Res.* **116**, D19121 (2011).
15. Trachsel, M. et al. Multi-archive summer temperature reconstruction for the European Alps. *Quat. Sci. Rev.* **46**, 66–79 (2012).
16. Nicholson, S. E., Dezfuli, A. K. & Klotter, D. A two-century precipitation dataset for the continent of Africa. *Bull. Am. Meteorol. Soc.* **93**, 1219–1231 (2012).
17. Muthers, S. et al. The coupled atmosphere–chemistry–ocean model SOCOL-MPIOM. *Geosci. Model Dev.* **7**, 2157–2179 (2014).
18. Sigl, M. et al. 19th century glacier retreat in the Alps preceded the emergence of industrial black carbon deposition on high-Alpine glaciers. *Cryosphere* **12**, 3311–3331 (2018).
19. Lüthi, M. P. Little Ice Age climate reconstruction from ensemble reanalysis of Alpine glacier fluctuations. *Cryosphere* **8**, 639–650 (2014).
20. Böhm, R. et al. The early instrumental warm bias: a solution for long central European temperatures series 1760–2007. *Clim. Change* **101**, 41–67 (2010).
21. PAGES 2k Consortium. Consistent multi-decadal variability in global temperature reconstructions and simulations over the common era. *Nat. Geosci.* https://doi.org/10.1038/s41561-019-0400-0 (2019).
22. Hawkins, E. et al. Estimating changes in global temperature since the preindustrial period. *Bull. Am. Meteorol. Soc.* **98**, 1841–1856 (2017).
23. Schurer, A. P., Mann, M. E., Hawkins, E., Tett, S. F. & Hegerl, G. C. Importance of the pre-industrial baseline for likelihood of exceeding Paris goals. *Nat. Clim. Change* **7**, 563–567 (2017).
24. Iles, C. & Hegerl, G. C. The global precipitation response to volcanic eruptions in the CMIP5 models. *Env. Res. Lett.* **9**, 104012 (2014).
25. Sontakke, N. A., Singh, N. & Singh, H. N. Instrumental period rainfall series of the Indian region (AD 1813–2005): revised reconstruction, update and analysis. *Holocene* **18**, 1055–1066 (2008).
26. Gallego, D., García-Herrera, R., Peña-Ortiz, C. & Ribera, P. The steady enhancement of the Australian summer monsoon in the last 200 years. *Sci. Rep.* **7**, 16166 (2017).
27. Hasselmann, K. Stochastic climate models part I. Theory. *Tellus* **28**, 473–485 (1976).
28. Yu, Y. et al. Observed positive vegetation–rainfall feedbacks in the Sahel dominated by a moisture recycling mechanism. *Nat. Commun.* **8**, 1873 (2017).
29. Held, I. M. et al. Probing the fast and slow components of global warming by returning abruptly to preindustrial forcing. *J. Clim.* **23**, 2418–2427 (2010).
30. Gupta, M. & Marshall, J. The climate response to multiple volcanic eruptions mediated by ocean heat uptake: damping processes and accumulation potential. *J. Clim.* **31**, 8669–8687 (2018).
31. Ding, Y. et al. Ocean response to volcanic eruptions in Coupled Model Intercomparison Project 5 simulations. *J. Geophys. Res. Oceans* **119**, 5622–5637 (2014).
32. Stenchikov, G. et al. Volcanic signals in oceans. *J. Geophys. Res.* **114**, D16104 (2009).
33. Gregory, J. M. et al. Climate models without preindustrial volcanic forcing underestimate historical ocean thermal expansion. *Geophys. Res. Lett.* **40**, 1600–1604 (2013).
34. Church, J. A. et al. in *Climate Change 2013: The Physical Science Basis* (eds Stocker, T. F. et al.) 1137–1216 (Cambridge Univ. Press, 2013).
35. Maher, N., McGregor, S., England, M. H. & Sen Gupta, A. Effects of volcanism on tropical variability. *Geophys. Res. Lett.* **42**, 6024–6033 (2015).
36. Mann, M. E. et al. Global signatures and dynamical origins of the Little Ice Age and medieval climate anomaly. *Science* **326**, 1256–1260 (2009).
37. Franke, J., Frank, D., Raible, C. C., Esper, J. & Brönnimann, S. Spectral biases in tree-ring climate proxies. *Nat. Clim. Change* **3**, 360–364 (2013).
38. Zumbühl, H. J., Nussbaumer, S. U., Holzhauser, H. & Wolf, R. *Die Grindelwaldgletscher—Kunst und Wissenschaft* (Haupt, 2016).
39. Nussbaumer, S. U., Zumbühl, H. J. & Steiner, D. Fluctuations of the Mer de Glace (Mont Blanc area, France) AD 1500–2050. Part I: the history of the Mer de Glace AD 1570–2003 according to pictorial and written documents. *Z. Gletsch. Glazialgeol.* **40**, 5–140 (2007).
40. Nussbaumer, S. U. & Zumbühl, H. J. The Little Ice Age history of the Glacier des Bossons (Mont Blanc massif, France): a new high-resolution glacier length curve based on historical documents. *Clim. Change* **111**, 301–334 (2012).
41. Küttel, M., Luterbacher, J. & Wanner, H. Multidecadal changes in winter circulation–climate relationship in Europe: frequency variations, within-type modifications, and long-term trends. *Clim. Dyn.* **36**, 957–972 (2011).
42. Brönnimann, S. et al. Causes for increased flood frequency in central Europe in the 19th century. *Clim. Past Discuss.* https://doi.org/10.5194/cp-2019-17 (2019).
43. Wegmann, M. et al. Volcanic influence on European summer precipitation through monsoons: possible cause for 'years without a summer'. *J. Clim.* **27**, 3683–3691 (2014).
44. Alfaro-Sánchez, R. et al. Climatic and volcanic forcing of tropical belt northern boundary over the past 800 years. *Nat. Geosci.* **11**, 933–938 (2018).
45. Gray, S. T., Graumlich, L. J., Betancourt, J. L. & Pederson, G. T. A tree-ring based reconstruction of the Atlantic Multidecadal Oscillation since 1567 AD. *Geophys. Res. Lett.* **31**, L12205 (2004).
46. Martin, E. R. & Thorncroft, C. D. The impact of the AMO on the West African monsoon annual cycle. *Q. J. R. Meteorol. Soc.* **140**, 31–46 (2014).
47. Krishnamurthy, L. & Krishnamurthy, V. Teleconnections of Indian monsoon rainfall with AMO and Atlantic tripole. *Clim. Dyn.* **46**, 2269–2285 (2016).
48. Brönnimann, S. et al. Southward shift of the northern tropical belt from 1945 to 1980. *Nat. Geosci.* **8**, 969–974 (2015).
49. Birkel, S. D., Mayewski, P. A., Maasch, K. A., Kurbatov, A. V. & Lyon, B. Evidence for a volcanic underpinning of the Atlantic Multidecadal Oscillation. *npj Clim. Atmos. Sci.* **1**, 24 (2018).
50. Anet, J. G. et al. Impact of solar versus volcanic activity variations on tropospheric temperatures and precipitation during the Dalton Minimum. *Clim. Past* **10**, 921–938 (2014).
51. Malik, A., Brönnimann, S. & Perona, P. Statistical link between external climate forcings and modes of ocean variability. *Clim. Dyn.* **50**, 3649–3670 (2018).
52. Hegerl, G. C., Brönnimann, S., Schurer, A. & Cowan, T. The early 20th century warming: anomalies, causes, and consequences. *WIREs Clim. Change* **9**, e522 (2018).
53. Brönnimann, S. Early twentieth-century warming. *Nat. Geosci.* **2**, 735–736 (2009).


## Acknowledgements

The work was supported by the Swiss National Science Foundation (projects 162668, 169676, CRSII2-147659 and a personal grant to M.T.), by MeteoSwiss (CH2018) and by H2020 (ERC Grant PALAEO-RA, 787574). Simulations were conducted at the Swiss Supercomputer Centre CSCS. G.C.H. and A.S. were supported by the ERC-funded project TITAN (EC-320691) and by NERC under the Belmont forum, grant PacMedy (NE/P006752/1).

## Author contributions

S.B. designed the study and performed most of the analyses. J.Franke performed the reanalysis. C.C.R. performed the FUPSOL model simulations and A.S. performed

the HadCM3 model simulations. C.C.R., A.M., M.W. and A.S. processed the model simulations. M.T. performed the temperature reconstruction. J.Franke and J.Flückiger performed some of the analyses, S.U.N., D.S. and H.J.Z. analysed the glacier data. G.C.H. assisted the analysis and interpretation of the model data. All the authors engaged in the discussion of the results and contributed to writing the paper.

## Competing interests

The authors declare no competing interests.

## Additional information

**Supplementary information** is available for this paper at https://doi.org/10.1038/s41561-019-0402-y.

**Reprints and permissions information** is available at www.nature.com/reprints.

**Correspondence and requests for materials** should be addressed to S.B.

## Methods

**Palaeo-reanalysis.** The palaeo-reanalysis EKF400 combines observations and proxies with an ensemble of 30 climate model simulations. The model used reconstructed sea-surface temperatures as the boundary conditions as well as external forcings, such as greenhouse gases and volcanic aerosols. The observations were assimilated using an off-line Ensemble Kalman Filter approach[13].

**Early instrumental observations.** We used all the series from the Global Historical Climatology Network monthly (version 3, adjusted)[14] with sufficient data (75% of the years must have data) in the reference period (1779–1808). To form a warm season average, 75% of the months must have data. To form an average of all the stations, 75% of the stations must have data. The stations used were Kremsmünster, Vienna, Prague, Paris, Karlsruhe, Berlin (two series), Munich, Hohenpeissenberg, Budapest, Milan, Turin, Vilnius, De Bilt, Trondheim, Warsaw, St Petersburg, Stockholm, Basel, Geneva, Edinburgh, Greenwich and New Haven.

**Model simulations.** *FUPSOL.* The ensemble simulations were based on the coupled atmosphere–chemistry–ocean model SOCOL-MPIOM (Solar Climate Ozone Links coupled to the Max Planck Institute Ocean Model)[17]. This is run in a horizontal resolution of approximately 3.5° with 39 levels up to 0.01 hPa. The four ensemble simulations from 1600 to 2000 are branched from the control simulation for perpetual 1600 conditions and the volcanic forcing set to zero. The control simulation still shows some drift of roughly 0.05 K per 100 yr and can be used to correct the variables. The four transient simulations are forced by greenhouse gas concentrations, volcanic aerosol and solar spectral irradiance, the former similar to the PMIP3 protocol[54], whereas the solar forcing is from Shapiro et al.[55], using the best estimate and the upper bound of the uncertainty. This results in a total solar irradiance change from the Maunder Minimum (1645–1715) to today of 6 W m$^{-2}$ (best estimate) and 3 W m$^{-2}$ (upper bound). Two ensemble members for each of the solar forcing settings were performed. A detailed description of the model and the simulations is given in Muthers et al.[17].

*HadCM3.* Ten ensemble members were run using the coupled atmosphere–ocean model HadCM3[56,57]. The atmosphere has a horizontal resolution of 3.75×2.5° in longitude and latitude with 19 levels. The ocean model has a resolution of 1.25×1.25° with 20 levels. The ensemble members were started in 1780 from the four all–forced and the four 'No aerosol direct effect' ensemble members described in Schurer et al.[11]. The simulations have very little drift and initial conditions that account for all known forcings starting in 800 AD[11]. The models were forced by PMIP3/CMIP5 protocol volcanic, solar, orbital and anthropogenic forcings as described in Schurer et al.[11]. The solar forcing used follows the Steinhilber et al.[58] data set, spliced into the Wang et al.[59] data set in 1810, and is therefore comparatively weaker than that used in the SOCOL-MPIOM model simulations. The volcanic forcing data set used is that of Crowley and Unterman[60]. The only forcing that is different to that described in Schurer et al.[11] is the anthropogenic aerosols, which were updated to follow the CMIP5 forcing following Smith et al.[61]. Note that some simulations only start in 1780, and hence 1780–1808 is used as reference in HadCM3.

**Volcanic eruptions.** We considered five eruptions in December 1808[8] (unknown), April 1815 (Tambora), October 1822 (Galanggung; note that this eruption was not part of the model forcing, including the model underlying the reanalysis), September 1831 (despite recent evidence of a possible misinterpretation of the 1831 Babuyan Claro eruption[9], we kept an eruption in that year due to enhanced sulfur in ice cores) and January 1835 (Cosigüina). Posteruption warm seasons are those that start within 30 months of the eruption, that is, 1809–11, 1815–17, 1823–25, 1832–33 and 1835–37 (for the December–February season in Fig. 3c the years are 1810–11, 1816–17, 1823–25, 1832–34 and 1836–37).

To composite the volcanic response in FUPSOL, in which only annual mean values are analysed, we considered all events in which the top-of-atmosphere net radiation exceeded −2 W m$^{-2}$ relative to our reference period 1779–1808 (this was considered as year 1). Twelve eruptions were selected in this way: 1600, 1641, 1673, 1693, 1719, 1761, 1808, 1815, 1831, 1835, 1884 and 1991. We then referenced all segments to year 0 (the pre-eruption year, which in no case rises above the background) and plotted years 0–10 (ending each segment when a new eruption started). The significance was calculated by the Monte Carlo sampling of segments over the 400 simulation years in the non-eruption parts of the time series, assuming the same eruption probability ($P$=0.03 yr$^{-1}$) as in the sample. This procedure was then repeated 100 times to obtain 95% confidence intervals. No confidence interval was calculated for Fig. 4d as the recovery of ocean heat content is so slow that no non-eruption parts can be defined.

**Multiproxy reconstructions of Alpine temperature.** Trachsel et al.[15] related six tree-ring chronologies from the Alpine area to the summer temperature from the HISTALP temperature data set[20] composed of early instrumental and instrumental temperature measurements that spanned the period 1760–2008. The reconstruction[15] is based on partial least squares (PLS) regression[62]. PLS is a regression technique based on a combination of dimension reduction and ordinary least squares (OLS) regression. In PLS the data set is divided into dependent and independent variables. In the dimension reduction step, a linear combination of dependent and independent variables is sought so that the correlation (or covariance) between the two linear combinations is maximized. The linear combination of the dependent variables is then related to the linear combination of the independent variables using OLS regression. In our reconstruction[15] there is only one dependent variable to which the linear combination of the independent variables is related using OLS regression.

Trachsel et al.[15] split the tree-ring and instrumental data into high- and low-frequency components. The low-frequency component was obtained using 31 yr low-pass filtered data (using a Gaussian filter) and the high-frequency component is the residual of the 31 yr low-pass filter (Trachsel et al.[15] gives a detailed description of the method).

For the high-frequency component, a normal OLS was used to relate the PLS scores (linear combination of the proxy data) to the instrumental data. A univariate linear regression is defined as:

$$y = \alpha + \beta\, x + e \tag{1}$$

$$e \sim N(0, \sigma^2) \tag{2}$$

where $x$ is the PLS score (linear combination of independent data), $y$ is the measured temperature data, $e$ is the residuals and $\sigma^2$ is the variance of the residuals. Model parameters were estimated in a Bayesian framework with uniform priors: $a \sim U(-\infty,\infty)$, $b \sim U(-\infty,\infty)$ and $s \sim U(0,\infty)$.

We then obtained predictions by sampling from the posterior predictive distributions[63]. In contrast to the high-frequency component, the low-pass filtered data set is temporally autocorrelated. Therefore, normal OLS is not an appropriate method to relate the PLS scores to instrumental data. Instead, we used a model with an autoregressive term of order 1 (AR1) and autocorrelated residuals:

$$y(t) = \alpha + \beta\, x(t) + \mathrm{ar1}\, y(t-1) + \varphi\, e(t-1) \tag{3}$$

where $x$ is the PLS score (linear combination of independent data), indices $t$ and $t-1$ are the value of a time series at time steps $t$ and $t-1$, $\beta$ is the parameter that relates the PLS scores to $y$, ar1 is the parameter that relates the value of $y$ at time step $t-1$ to the value of $y$ at time step $t$ and $\varphi$ is the parameter that relates the residual at time step $t-1$ to the residual at time step $t$. This model was run in a Bayesian framework using uniform priors for all the parameters. To give some weight to the PLS scores, the prior of ar1 was:

$$\mathrm{ar1} \sim U(-0.65, 0.65) \tag{4}$$

Both regression models (equations (1) and (3)) were run in a Bayesian framework, with three chains of 11,000 iterations with 1,000 iterations for adaptation (burn in) and a thinning interval of 10. This resulted in 3,000 climate histories of low and high frequency. Combining all these histories resulted in an exceedingly large sample size of nine million histories. Therefore, 100 histories of each component were chosen and all their possible 10,000 combinations (that is, sums) were assessed.

These 10,000 internally consistent reconstructions were then smoothed with a 30 yr running mean filter, which resulted in an ensemble of smoothed reconstructions. The 2.5% and the 97.5% quantiles of these 30 yr smoothed reconstructions were then used as confidence bounds for the 30 yr smoothed reconstruction.

**Cyclone track.** To study the strength and position of the cyclone track over Europe we analysed daily or subdaily pressure data from 13 stations[64,65]: Amsterdam (4.9° E, 52.37° N), Armagh (6.64° W, 54.35° N), Basel (7.59° E, 47.56° N), Bern (7.45° E, 46.95° N), Geneva (6.14° E, 46.2° N), Great St Bernard (7.19° E, 45.89° N), London (0.12° W, 51.51° N), Milan (9.19° E, 45.46° N), Paris (2.35° E, 48.86° N) Stockholm (18.06° E, 59.33° N), Turin (7.74° E, 45.12° N), Uppsala (17.63° E, 59.86° N) and Zurich (8.54° E, 47.38° N). We used a 2–6 d bandpass Lanczos filter[66] with a 31 d convolution vector (as in Brugnara et al.[64]). The results were then expressed as anomalies from a 1961–1990 climatology from the closest grid point in the Twentieth Century Reanalysis 20CRv2c[67].

**Circulation indices.** We analysed two zonal mean circulation indices from the palaeo-reanalysis. The positions of the northern subtropical jet and of the downwelling branch of the northern Hadley were determined as the position of the maximum zonal average zonal wind at 200 hPa and the position of the maximum zonal mean omega at 500 hPa, respectively, as described in in Brönnimann et al.[48] (we used the same settings as described for the SOCOL model simulations).

## Data availability

The palaeo-reanalysis is available from http://cera-www.dkrz.de/WDCC/ui/Compact.jsp?acronym=EKF400_v1.1 and instrumental temperature data from https://www.ncdc.noaa.gov/ghcnm/v3.php. The dryness indices for Africa are available from https://www1.ncdc.noaa.gov/pub/data/paleo/historical/africa/africa2001precip.txt

and the Australian monsoon data from https://www.upo.es/vareclim/Data/Data_Index.php. The pressure data used are available from ISPD, https://reanalyses.org/observations/international-surface-pressure-databank. FUPSOL and HadCM3 model output can be downloaded from https://boris.unibe.ch/131129/.

## Code availability

Code for the calculation of subtropical jet latitude and northern topical edge is from https://boris.unibe.ch/71204/. Code and input data for the reconstruction of Alpine summer temperature can be downloaded from https://boris.unibe.ch/131129/.

## References


54. Braconnot, P. et al. Evaluation of climate models using palaeoclimatic data. *Nat. Clim. Change* **2**, 417–424 (2012).
55. Shapiro, A. I. et al. A new approach to long-term reconstruction of the solar irradiance leads to large historical solar forcing. *Astron. Astrophys.* **529**, A67 (2011).
56. Pope, V. D. et al. The impact of new physical parametrizations in the Hadley Centre climate model: HadAM3. *Clim. Dyn.* **16**, 123–146 (2000).
57. Gordon, C. et al. The simulation of SST, sea ice extents and ocean heat transports in a version of the Hadley Centre coupled model without flux adjustments. *Clim. Dyn.* **16**, 147–168 (2000).
58. Steinhilber, F., Beer, J. & Fröhlich, C. Total solar irradiance during the Holocene. *Geophys. Res. Lett.* **36**, L19704 (2009).
59. Wang, Y.-M., Lean, J. L. & Sheeley, N. R. Modeling the Sun's magnetic field and irradiance since 1713. *Astrophys. J.* **625**, 522–538 (2005).
60. Crowley, T. J. & Unterman, M. B. Technical details concerning development of a 1200-yr proxy index for global volcanism. *Earth Syst. Sci. Data* **5**, 187–197 (2013).
61. Smith, D. M. et al. Improved surface temperature prediction for the coming decade from a global climate model. *Science* **317**, 796–799 (2007).
62. Martens, H. & Naes, T. *Multivariate Calibration* (Wiley, 1989).
63. Kruschke, J. *Doing Bayesian Data Analysis. A Tutorial with R, JAGS, and Stan* (Academic, 2014).
64. Brugnara, Y. et al. A collection of sub-daily pressure and temperature observations for the early instrumental period with a focus on the 'year without a summer' 1816. *Clim. Past* **11**, 1027–1047 (2015).
65. Cram, T. A. et al. The international surface pressure databank version 2. *Geosci. Data J.* **2**, 31–46 (2015).
66. Duchon, C. E. Lanczos filtering in one and two dimensions. *J. Appl. Meteorol.* **18**, 1016–1022 (1979).
67. Compo, G. P. et al. The twentieth century reanalysis project. *Q. J. R. Meteorol. Soc.* **137**, 1–28 (2011).